Article

How Wetting and Drainage Cycles and Wetting Angle Affect Capillary Air Trapping and Hydraulic Conductivity: A Pore Network Modeling of Experiments on Sand

Tomas Princ [1], John Koestel [2,3] and Michal Snehota [1,4,*]

1 Faculty of Civil Engineering, Czech Technical University in Prague, 166 29 Prague, Czech Republic; princ.tomas@vumop.cz
2 Department of Soil and Environment, Swedish University of Agricultural Sciences, 750 07 Uppsala, Sweden; john.koestel@slu.se
3 Soil Quality and Soil Use, Agroscope, 8046 Zürich, Switzerland
4 University Centre for Energy Efficient Buildings, Czech Technical University in Prague, 273 43 Bustehrad, Czech Republic
* Correspondence: michal.snehota@cvut.cz

Abstract: Entrapped air in porous media can significantly affect water flow but simulations of air entrapment are still challenging. We developed a pore-network model using quasi-static algorithms to simulate air entrapment during spontaneous wetting and subsequent drainage processes. The model, implemented in OpenPNM, was tailored to replicate an experiment conducted on a medium-sized unconsolidated sand sample. We started building the model with three types of relatively small networks formed by 54,000 pore bodies which we used to calibrate basic network topological parameters by fitting the model to the water retention curve and the saturated hydraulic conductivity of the sand sample. Using these parameters, along with X-ray image data (μCT), a larger network formed by over 250,000 pore bodies was introduced in the form of stacked sub-networks where topological parameters were scaled along the z-axis. We investigated the impact of two different contact angles on air entrapment. For a contact angle of 0, the model showed good agreement with the experimental data, accurately predicting the amount of entrapped air and the saturated hydraulic conductivity. On the contrary, for a contact angle of $\pi/4$, the model provided reasonable accuracy for saturated hydraulic conductivity but overestimated the amount of entrapped air. Overall, this approach demonstrated that a reasonable match between simulated and experimental data can be achieved with minimal computational costs.

Keywords: capillary trapping; residual saturation; entrapped air; pore-network model; spontaneous imbibition; satiated hydraulic conductivity

1. Introduction

It has been experimentally demonstrated that entrapped air in a non-wetting phase strongly affects water flow through porous media [1,2]. In particular, the presence of entrapped air in preferential flow pathways of soil can create obstructions that significantly reduce the overall flow of water [3–5].

Recent advances in imaging techniques, such as X-ray microtomography, have provided deeper insights into the morphology of residual non-wetting phases [6]. For instance, Scanziani et al. [7] utilized this technique to visualize the dynamics of gas trapping in CO_2 storage scenarios, emphasizing the role of the pore structure in influencing the trapping efficiency. Wang et al. [8] demonstrated that both water-wet and CO_2-wet conditions enhance the trapping of CO_2 compared to weakly water-wet or neutral conditions.

Continuum models mainly implement entrapment and fate of air using the two-phase (or multiphase) flow approach [9,10]. It has frequently been assumed that the residual air

content is constant, but this assumption is often not valid [11,12]. Alternatively, pore-scale models take the three-dimensional geometry of the pore network into account. Various pore-scale modeling approaches have been used in the past, such as the volume-of-fluid method [13,14], the lattice Boltzmann method [13,15], and pore-network modeling [16,17]. The volume-of-fluid and lattice Boltzmann methods are computationally demanding, and they have typically been used to describe only small domains of the order of several pore bodies in each direction [18].

Pore network models (PNMs) have been shown to successfully and efficiently predict numerous aspects of multiphase flow and transport processes in porous media [19–23]. Algorithms used in PNMs are often based on percolation theory [22,23], which simulate processes based on physical forces [24–27] that require little computational power and time [21,28,29]. A thorough overview of PNMs has been given in seminal works by Blunt et al. [19] and Sahimi [30].

The geometry and topology of the pore network are key parameters of PNMs [31]. The topology of the network determines the location of pore bodies and their connection through pore throats. Early studies used pore throats and pore bodies with circular cross sections [32,33]. Such approaches are being increasingly replaced by pore throats and pore bodies with angular cross sections (triangle, square, hyperbolic polygons, etc.), which allow simulations of corner flow [34]. The geometry and topology of the pore network can be constructed as random computer-generated structures [35–37] or can be derived directly from highly resolved image data of porous media [38,39]. The pores network generated based on high resolution 3D images, mostly obtained by X-ray imaging on synchrotrons provide the most realistic description [40–42], albeit only for sample volumes ranging from several cubic millimeters [41] to several cubic centimeters [43]. The small size of the domain is a disadvantage when investigating the hydraulic properties of complex porous media such as soils, which often require larger sample sizes to meet the prerequisites of a representative elementary volume.

The purpose of this study was to develop and parameterize a pore network model using the OpenPNM platform [44] to simulate air entrapment and water flow through coarse sand during repeated wetting and drainage cycles. Specifically, we sought to determine if a pore network constructed on (i) the water retention curve and (ii) the saturated hydraulic conductivity of the porous material, as well as (iii) the average diameter of entrapped air bubbles with depth obtained from X-ray image data could provide a representation of the experimental data on wetting and draining.

2. Materials and Methods

2.1. Model Background

2.1.1. Network Generation

The model presented is based on the OpenPNM framework [44]. This open-source package has previously been used to characterize diffusivity in the thin, porous layer [45] or to solve multiphase transport through the fuel cell [46,47].

The generated networks comprised interconnected pore bodies and pore throats, both a square cross-section. The network topology is defined by the coordinates of the pore bodies and a list of pairs of pore bodies connected by the corresponding pore throats. One of the parameters that describe the network is the coordination number z (-). The value z indicates the average number of pore throats connected to a single pore body. Another parameter, the aspect ratio, indicates the ratio between the pore body and the radius of the pore throat.

2.1.2. Physics Considered in the Simulation Model

We simulated both the drainage and wetting of water in the sand sample as a flow of an invading fluid phase towards a defending phase that is initially present in the network. This process is described by invasion percolation and simulated by considering two key

parameters: the entry pressure and the conductivity of the individual network elements, namely the pore bodies and throats.

The entry pressure of the element corresponds to the capillary pressure (difference between the non-wetting and wetting phase pressures) at which the invading phase begins to enter the element filled by the defending phase. During drainage, when the capillary pressure drops, it eventually falls below the entry pressure of the element, then the element is filled by the non-wetting (invading) phase by a piston-like displacement. During the imbibition process, the capillary pressure increases, which leads to the filling of the element with the wetting phase when the entry pressure of the element is exceeded.

Our simulation model was based on a simplified representation of the porous medium using percolation theory. We assumed that only pore throats were relevant for the drainage process. The simplification is applicable because the entry pressure of the pore throat is generally lower than the entry pressure of the pore body because the size of the throat is smaller than the size of the pore body. Therefore, when a pore throat is drained, it means that the adjacent pore body also drains. However, capillary pressure increases during imbibition. In this way, elements with a smaller radius and lower entry pressure are saturated preferably, from which it follows that the pore bodies are more important for the imbibition process.

The entry pressure of a pore throat with a regular polygon cross section is described by Equation (1) [48]:

$$P_{e,t} = \frac{\sigma}{r_t} \left\{ \cos \theta + \sqrt{\frac{\tan \alpha_c}{2} \left(\sin 2\theta + \pi - 2(\alpha_c + \theta) \right)} \right\} \tag{1}$$

where r_t (m) is the inscribed radius of the pore throat, θ (rad) is the contact angle, and α_c (rad) is the half-angle of the corners ($\pi/4$ for square).

For the imbibition algorithm, the entry pressure of the pore body, $P_{e,p}$ (Pa), depends on the geometrical characteristics which determine the radius of curvature of the interface R_n (m):

$$P_{e,p} = \frac{2\sigma}{R_n} \tag{2}$$

where σ (N·m^{-1}) is the interfacial tension. The radius of curvature was determined following [49], based on the calculation of the entry pressure for a spherical pore body. The relationship is identical for a cubic pore body since the interface geometry remains the same (see Figure 1a). The pore bodies filled with the non-wetting phase with a maximum angular pitch of their axes (α_p in Figure 1a) were used to calculate R_n. If there was more than one combination of throats with the same maximum angular pitch, then the combination with larger throats was used. The radius of curvature of the interface (R_n) for throats with equal radii was determined by Equation (3):

$$aR_n^2 + bR_n + c = 0 \tag{3}$$

where:

$$a = \left(cos\beta_S + \frac{sin\beta_S}{tan\frac{\alpha}{2}} \right)^2 - 1 \quad b = -2 \left(cos\beta_S + \frac{sin\beta_S}{tan\frac{\alpha}{2}} \right) \left(\frac{r_t}{sin\frac{\alpha}{2}} + R_p cos\frac{\gamma}{2} \right) \quad c = \left(\frac{r_t}{sin\frac{\alpha}{2}} + R_p cos\frac{\gamma}{2} \right)^2 + \left(R_p sin\frac{\gamma}{2} \right)^2 \tag{4}$$

where R_p (m) is pore body radius, γ (rad) is selected as α_p as discussed in [49], and $\beta_S = \pi/2 - \theta - \alpha_p$ (rad). When the pore throats were of different radii, the equivalent pore radius was determined according to [49] using the smaller of the two pore throat radii, and the value of angular space remained α_p. The entry pressure was then determined by Equations (2)–(4) with the equivalent parameters.
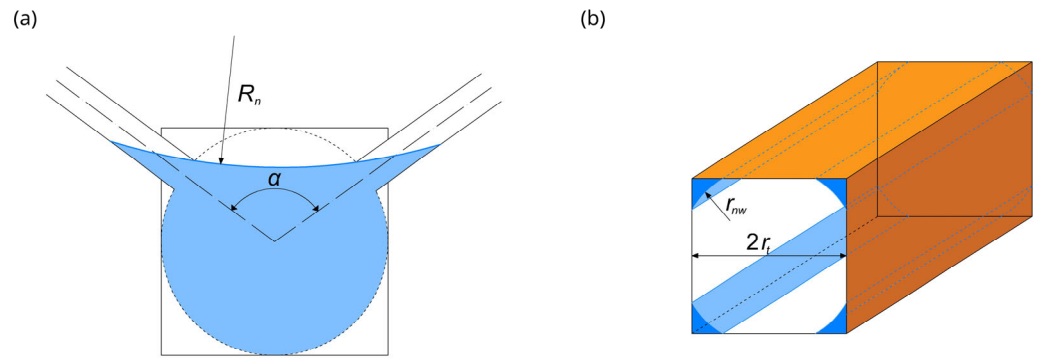
Figure 1. Diagram of the geometry used in the PNM. (**a**) A pore body with two identical pore throats with angular pitch α_p and interface radius R_n [49] Cubic and spherical pore body geometries are shown. (**b**) A cross-section of the square pore throat with the radius of the inscribed circle r_t and with the water film with the radius of curvature r_{nw} in the corners.

In addition, the capillary pressure within the pore network changes hydrostatically with elevation in the gravitational field. Hydrostatic pressure was accounted for by changing the entry pressure according to height.

$$P_{e\_fin,el} = P_{e,el} - \rho_w g z_{el} \tag{5}$$

where $P_{e\_fin,el}$ (Pa) is the final entry pressure of element *el*, ρ_w (kg·m^{-3}) is the density of the water, and z_{el} (m) is the height of the center of the element *el* from the bottom of the pores network.

Furthermore, the capillary pressure applied during drainage, P_c^* (Pa), is suitable for calculating the radius of curvature of the water film in the corners of the pore throats and bodies (Figure 1b):

$$r_{nw} = \frac{\sigma}{P_c^*} \tag{6}$$

The area of water in the cross-section, A_w (m^2), is determined by

$$A_w = N_c r_{nw}^2 \left[\frac{\cos\theta}{\sin\alpha_c} \cos(\alpha_c + \theta) - \frac{\pi}{2} + \alpha_c + \theta \right] \tag{7}$$

where N_c (-) is the number of corners, and the air volume in the whole element, V_g (m^3), is:

$$V_g = V_e - V_w = V_e - \frac{A_w}{A_e} V_e \tag{8}$$

where A_e (m^2) is the area of the cross-section of the element, V_e (m^3) is the volume of the element, and V_w (m^3) is the volume of the water film. For the water film to form in the corners, the condition of $\theta < \pi/2 - \alpha_c$ must be met.

We assumed the Poiseuille law in each pore throat to calculate its hydraulic conductivity [50]. The flow rate of the wetting phase from the pore body *i* to an adjacent pore body *j*, q_{ij} (m^3·s^{-1}), was determined as follows:

$$q_{ij} = g_{ij} \Delta P_{ij} \tag{9}$$

where ΔP_{ij} (Pa) is the difference between the pressure of the wetting phase in the pore bodies *i* and *j*, and g_{ij} (m^3·Pa^{-1}·s^{-1}) is the throat hydraulic conductivity of the pore throat

that connects *i* and *j*. The conductivity of the throat for single-phase flow, when the throat was filled by the wetting phase, was:

$$g_{ij}^{w,1-p} = \frac{\pi r_{eff}^4}{8\mu_w l} \tag{10}$$

where r_{eff} (m) is the hydraulic radius, μ_w (Pa·s) is the dynamic viscosity of the wetting phase, l (m) is the length of the throat, and the superscript $w, 1-p$ indicates the single-phase water flow. The hydraulic radius was determined following Bryant and Blunt [51]:

$$r_{eff} = \frac{\sqrt{A_t/\pi} + r_t}{2} \tag{11}$$

where r_t (m) is the inscribed radius of the pore throat, and A_t is the area of the cross-section of the pore throat. The wetting phase conductivity of an unsaturated pore throat (water flow in corner water films) is given by [52]:

$$g_{ij}^{w,2-p} = \frac{A_w r_{nw}^2}{\beta \mu_w l} \tag{12}$$

where the superscript $w, 2-p$ indicates two-phase water flow, and the resistance factor β (-) was determined by Equation (13) according [53]:

$$\beta = \frac{12 \sin^2 \alpha_c (1-B)^2 (\psi_3 + fB\psi_2)^2}{(1-\sin \alpha_c)^2 B^2 (\psi_1 - B\psi_2)^2} \tag{13}$$

where its coefficients are

$$\psi_1 = \cos^2(\alpha_c + \theta) + \cos(\alpha_c + \theta)\sin(\alpha_c + \theta)\tan \alpha_c, \quad \psi_2 = 1 - \frac{\theta}{\frac{\pi}{2} - \alpha_c}$$
$$\psi_2 = 1 - \frac{\theta}{\frac{\pi}{2} - \alpha_c}, \quad \psi_3 = \frac{\cos(\alpha_c + \theta)}{\cos \alpha_c} \tag{14}$$
$$B = \left(\frac{\pi}{2} - \alpha_c\right)\tan \alpha_c$$

here the $f = 0$.

Appendix A describes both existing and new algorithms used in pore network modeling.

2.2. Experiments Carried Out on Sand Columns

We conducted two different experiments on columns packed with the same coarse sand. The first was the measurement of the primary drainage branch of the water retention curve on the sand column performed using the sandbox apparatus [54].

The second experiment [55] consisted of a series of drainage–imbibition cycles to study the relationship between the entrapped volumetric air content and the saturated and satiated hydraulic conductivity (Figure 2a).

The material used in this study was coarse sand (ST 03/08, Sklopisek Strelec, Czech Republic). Particle sizes ranged from 0.1 to 1.0 mm. The value of the uniformity coefficient (D_{60}/D_{10},) was 2.2 and the effective particle size (D_{10}) was 0.29 mm. The particle density was 2.62 g·cm^3. The dry bulk density of the sample was calculated from the mass and volume of the dry sand sample (1.67 g·cm^3). Sample porosity was determined from particle density and the dry bulk density (0.354 cm^3·cm^{-3}).

The water retention curve was used to fit the van Genuchten model [56], where we found the parameters $\alpha = 0.048$, $n = 3.976$, $m = 0.749$.

The second experiment started with a sand sample that had been fully saturated in a vacuum chamber. The value of ω_r was assumed to be equal to 0 due to full saturation. The saturated hydraulic conductivity (K_s) was determined by repeating the fall-head method. (Figure 2b) with manual additions of 40 cm^3 dose of water each time the water level dropped to the pin. The constant water level was kept around the sample by continuously removing excess water using a pump. The measurement was repeated ten times.
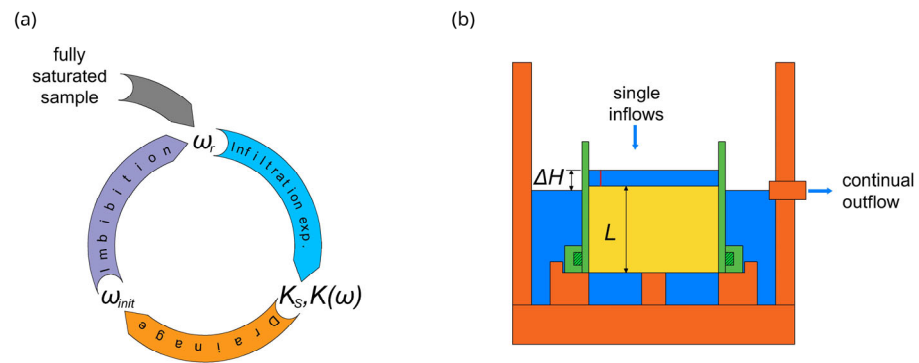
Figure 2. Description of the second experiment. (**a**) Cycle of the second experiment. The infiltration experiment served to obtain hydraulic conductivities (K_S, $K(\omega)$). Then, the pressure head for the drainage was set at a new value between 4 and 50 hPa of suction pressure. After the drainage process, the value of ω_{init} was determined as the initial volumetric air content before the entrapment of air took place during imbibition. The spontaneous imbibition was carried out from the bottom of the sample and then the amount of entrapped air, ω_r, was determined. (**b**) Experimental setup. The vessel is represented by an orange color, and the container with the sample is shown in green. A pin (red) was placed on top of the sand column (yellow) that served as a marker enabling it to maintain a constant ponding depth at the start of the saturated hydraulic conductivity measurement.

The mass of fully saturated sand was recorded and was later used as a reference for gravimetric measurements of the entrapped air content.

The drainage and spontaneous imbibition cycles were performed (Figure 2a). Drainage was carried out on a sand table with the given pressure head. The value of ω_{init} was obtained gravimetrically, by weighing the container with the sand column after drainage. Imbibition after each drainage step was performed by flooding the sample upwards through the bottom. By filling the outer container to the standard level, it was possible for each step to determine the mass of water replaced by the trapped air relative to the initial fully saturated state and to calculate ω_r. The satiated hydraulic conductivity (hydraulic conductivity at the actual residual gas saturation) $K(\omega)$ was measured after each imbibition using the same falling head method as used for the measurements of K_s. A total of ten drainage and imbibition cycles were completed. Furthermore, three-dimensional X-ray μCT images of the sample in the drained and flooded (saturated or satiated) states were recorded for two additional cycles. The experiments were detailed in [55].

2.3. Description of Numerical Simulations

Two contact angle values were considered for the simulations. The first contact angle $\theta = \pi/4$ represents weakly wet conditions. This value was selected to represent a realistic value for the coarse sand. It is still small enough to prevent snap-off effects. Snap-off cannot occur for $\theta = \pi/4$, due to the condition of $\theta < \pi/2 - \alpha_c$ required for the creation of water film, because the water will not adhere in the corners [52]. The second value of θ was chosen to be 0, which well represents the state of very wet sand. Both θ-values were used for generating networks and simulations.

2.3.1. Small Networks Generation

A uniform network of $30 \times 30 \times 60$ pore bodies was generated which has been shown to be a sufficient size for this purpose [31]. Because hydraulic characteristics mainly depend on the topology of the pore network and size distribution of the pore network elements, three different approaches for pore network generation were used.

The first network type was a cubic network with a connectivity equal to 6 and a *spacing* of 180 μm, with the truncated Weibull distribution of pore body radii:

$$R_p = (R_{max} - R_{\min})\left(-\sigma\ln\left(x\left(1 - e^{-\frac{1}{\sigma}}\right) + e^{-\frac{1}{\sigma}}\right)\right)^{\frac{1}{\delta}} + R_{min} \tag{15}$$

where x (-) was a random number between 0 and 1. Parameters of this network were the minimal radius, R_{min} (m), the maximal radius, R_{max} (m), and the parameters σ (-) and δ (-).

The second network was a cubic network constructed with a connectivity equal to 26 and a spacing of 180 μm. The connectivity was then randomly reduced for the entire network to an integer value of the coordination number z between 4 and 8. Again, the Weibull distribution of the pore body radii was used (15). The parameters of this network type were R_{min}, R_{max}, σ, δ and z.

The third network type had a random spatial distribution of the pore body centers; the number of pores bodies was N_p (). The throats that connected the pore bodies were generated by the OpenPNM *Gabriel* algorithm. The maximum radius of the pore bodies was determined. Then the radius of each pore body was determined from the maximum radius by multiplying by the coefficient ε (-), which was constant for the entire network. The value of ε varied from {0.5, 0.7, 0.9}. The parameters of the network were ε and N_p.

The radius of the throat was determined from the radii of the pore bodies adjacent to the addressed throat (R_{p1} and R_{p2}) as

$$r_t = C\min\left(R_{p1}, R_{p2}\right) \tag{16}$$

where the value of constriction factor C (-) was randomly selected from {0.80, 0.85, 0.90}.

2.3.2. Simulations in Small Networks

The drainage algorithm was used to simulate the sand retention curve to match it with the measured retention curve. The results of these backward simulations were two networks (parameters), one for the $\theta = 0$ and the other for the $\theta = \pi/4$. Hundreds of network realizations were generated for each network type and each contact angle.

The pressure head boundary was established at the bottom of the network, while air entered from the top. Saturated hydraulic conductivity was determined for each network ($K_{s,s}$). Six measured points of the retention curve (suction pressure at: 15, 25, 30, 35, 40, and 50 hPa) were used for the comparison of the measured and simulated curves. The objective function for parameter optimization φ (-) was:

$$\varphi = \sum_{i=1}^{6} (VWC_s(h_i) - VWC_m(h_i))^2 + 2(p_s - p_m)^2 + 2(K_{s,s} - K_{s,m})^2 \tag{17}$$

where VWC_s (-) and VWC_m (-) are simulated and measured volumetric water content, respectively, each corresponding to specific pressure head h_i. Parameters p_s (-) and p_m (-) are porosities, obtained from the simulation and from the measurement. The $K_{s,s}$ and $K_{s,m}$ are the (fully) saturated hydraulic conductivities, obtained from simulation and measurement.

The above-described network parameterization steps were carried out for two contact angles on all three considered network types. First, we parameterized three small network models using a contact angle $\theta = 0$. Subsequently, we repeated the parameterization for a contact angle of $\theta = \pi/4$, yielding another set of three small network models. After obtaining the network parameters, the retention curve based on the parameterized pore network models was calculated for the range of 5 to 50 hPa in small pressure head steps ($\approx$2 hPa). A total of 20 unique network replicates were generated using the best-fitting parameters for each contact angle for the cubic regular approach. The retention curve was simulated for each network.

Furthermore, the relationships between the residual gas saturation of the sample, $S_{g,r}$ (-), and initial gas saturation, $S_{g,init}$ (-), were calculated and plotted for 5 unique networks with best-fitting parameter replicates. The values of $S_{g,r}$ resp. $S_{g,init}$ were obtained from the values of ω_r resp. ω_{init} by dividing porosity. The suction pressure values were {25, 28, 30, 32, 35, 40, 45, 50} hPa for networks generated for $\theta = 0$ and {20, 21, 22, 25, 26, 27, 28, 30, 35, 40, 50} hPa for the networks generated for $\theta = \pi/4$. First, a drainage simulation was performed with the lower pressure head boundary condition set at the bottom of the

network and the air inlet located at the top of the network. The value of ω_{init} (and the derived value of $S_{g,init}$) was a result of this step. Subsequently, the imbibition algorithm with inflow from the bottom of the network was used. Then the trapping algorithm was used to obtain the value of ω_r (and the derived value of $S_{g,r}$). This was repeated for all pressure head values.

2.3.3. Large Network Generation

The generation of the network was aided by additional information provided by μCT of the sample. The μCT images showed that large globular air-filled pores were formed in the upper part of the sample during drainage–imbibition cycling probably by air bubbles, while the lower part remained mostly unaffected by bubble formation. Thus, the network parameters in the bottom most part (sub-network 1) were kept the same as in simulation in a small network (Section 2.3.2), while the pore network parameters were modified in the rest of the network. The resulting large pore network consisted of nine sub-networks, small pore networks stacked on top of each other, where pore-network elements size increased with increasing elevation (Figure 3a). These sub-networks represented sub-volumes of the sub-volumes of the μCT image of the sample. The size of the largest bubbles, and thus also the largest pore bodies, was determined from the μCT images for each sub-volume. This information was also used to build the pore network. An example of a cross section with region of interest in the upper half of the sand sample (height is from 25 to 50 mm) is shown in Figure 3a.
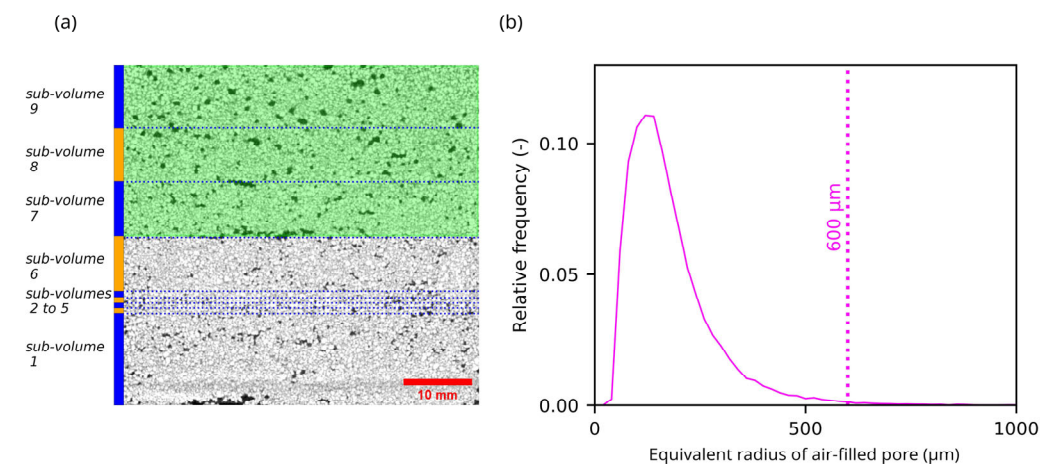

Figure 3. Description of the procedure in which the maximal μCT determined air-filled pore radius was obtained from μCT images. (**a**) Example of μCT vertical cross section. Air-filled pores are presented in black color. The region of interest used for the calculation of the largest bubble-formed pore is the upper half of the sample (the green region). The sub-volumes numbered from 1 to 9 are sub-networks represented in the model by different parameters of the pore network. (**b**) Histogram of the μCT determined air-filled radii formed by air bubbles obtained for the upper half of the sand sample. The radius was determined from the volume of μCT determined air-filled pores with the assumption of its spherical shape.

The network parameters R_{min}, R_{max} and *spacing* were kept constant within each individual sub-network but increased linearly with increasing distance of the sub-network above the base of the large network, in the same fashion as in the acquired sub-volumes of μCT images. The ratio between these parameters remained constant. The parameters σ and δ were kept constant throughout the pore network. Sub-networks 2–5 were more densely spaced to achieve a smoother transition between sub-network 1 and sub-network 6.

The histogram of μCT determined air-filled pores radii in the upper half of the sample is shown in Figure 3b. Air-filled pores radii were determined from the segmented μCT image as pore volumes with the assumption of the spherical shape of the pores. The maximal

pore body radius was specified as 600 μm with the assumption that 1% represented outliers (Figure 3b). The radius of the pore throat (radius of the inscribed circle) was determined.

$$R_t = C^* \min(R_{p1}, R_{p2}) \tag{18}$$

where the constriction factor of the large network C^* (-) was kept constant and R_{p1}, R_{p2} were the radii of the pore bodies adjacent to the addressed pore throat.

2.3.4. Simulations in a Large Network

The simulation of the experiment involved two steps. The first step was the drainage simulation, performed on an initially fully saturated sample using a drainage algorithm with a boundary condition of −30 hPa pressure at the bottom.

The second step involved simulation of the imbibition using an algorithm with the input at the bottom. The order in which the pores were filled obtained from the imbibition algorithm was used as input for the entrapment algorithm, which eventually provided the set of pores occupied with trapped air. The air leak outlet was positioned at the top of the network and residual gas saturation was determined. Finally, the last algorithm was utilized to determine the satisfied hydraulic conductivity.

The result of the simulation was a histogram of the sizes of the air groups trapped. In addition, the frequency of the clusters that correspond to the ganglia was determined. Whether the given cluster represented a ganglion was decided using a topological parameter, the Euler number, which was calculated using the equation described by [31].

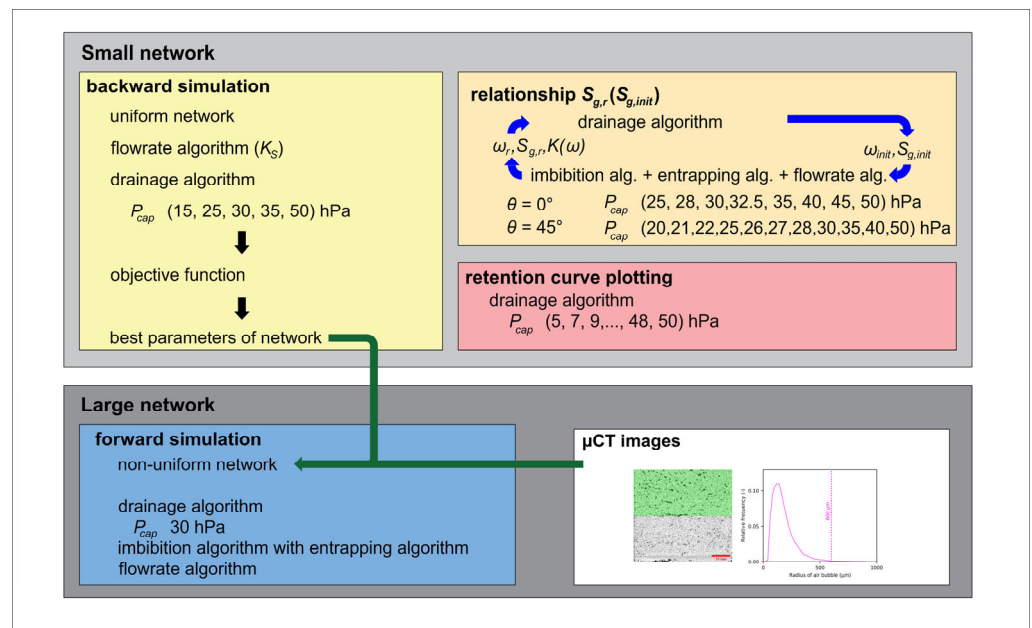Figure 4 shows the schema of simulation processes for both small and large networks.

Figure 4. Schema of simulation processes, in the upper part, the simulations are described in a small network, and in the lower part the simulations are described in a large network.

3. Results and Discussion

3.1. Generated Networks

The comparison of the results obtained using different networks for the numerical experiment in small networks is shown in Figure 5. The saturated hydraulic conductivity, porosity, and objective function were obtained for each of the networks. Each point in Figure 5 corresponds to the results obtained from one network. The points in Figure 5c,f form three separate groups that reflect the value of ε, shown in Figure 5c. Additionally, smaller subgroups, which correspond to different values of C, are visible in each group.
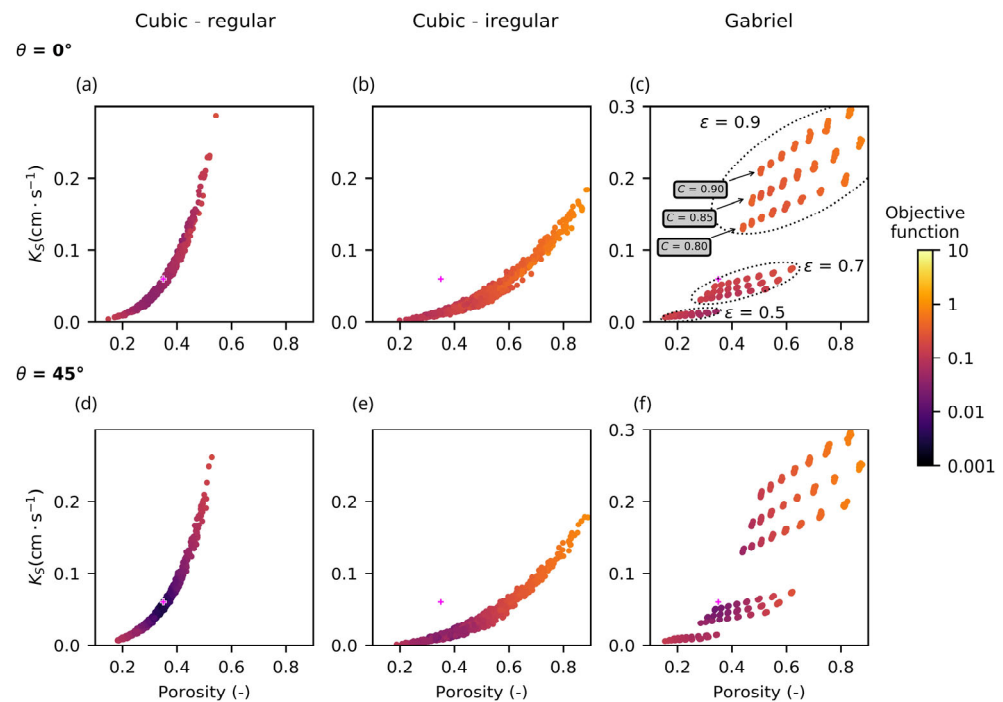
Figure 5. Comparison of the results simulated for three pore network configurations. The columns (**a**,**d**), (**b**,**a**), (**c**,**f**) correspond to the three network generation approaches and the rows (**a**–**c**), (**d**–**f**), correspond to the two values of the contact angle. The magenta cross symbol shows the K_s values determined in laboratory experiment. The color of the other points represents the value of the objective function φ. The plots with the results of Gabriel's approach exhibited a higher range of K_S values.

The regular cubic and Gabriel method-generated networks led to simulated hydraulic conductivities similar to the measured one. However, the use of a regular cubic approach led to the lowest value of the objective function. In the case of contact angle 0 the network generation parameters that led to the best fit of the pore network model to the measured retention curve and K_s were R_{min} = 6.4 μm, R_{max} = 86.6 μm, σ = 1.3931, and δ = 1.0308 which leads to simulated porosity 0.321 and K_s = 0.045 cm·s^{-1}. In the case of the contact angle $\pi/4$ the optimal parameters were R_{min} = 14.6 μm, R_{max} = 86.1 μm, σ = 1.0071, and δ = 1.0073 leading to simulated porosity 0.353 and K_s = 0.058 cm·s^{-1}. The optimized value of parameter C was 0.9 in both cases.

Network parameter sets were further used for generating sub-network 1 for the large pore network for the forward simulation. The values of the network parameters are listed in Table 1. The value of C^* equal to 0.93 (Equation (18)) led to porosities of the whole sample equal to 0.35 for $\theta = \pi/4$ and 0.32 for $\theta = 0$. The pore network for this numerical experiment was constructed from 253,146 pore bodies and 744,360 pore throats.

Table 1. Parameters of 9 sub-networks of connected cubic networks. Sub-network 1 is the bottom layer and sub-network 9 is the top layer of the large network. The remaining parameters were $C^* = 0.93$, $\sigma = 1.3931$, and $\delta = 1.0308$ for $\theta = 0$, and $C^* = 0.93$, $\sigma = 1.0071$, and $\delta = 1.0073$ for $\theta = \pi/4$.

Sub-Network	R_{min}		R_{max}		Spacing	Height	Width
$\theta =$	0	$\pi/4$	0	$\pi/4$	$0/\pi/4$	$0/\pi/4$	$0/\pi/4$
	(µm)		(µm)		(µm)	(pores)	(pores)
Simulation in a small network							
-	6.4	14.6	86.6	86.1	180	60	30
Simulation in a large network							
1	6.4	14.6	86.6	86.1	180	75	50
2	6.8	15.4	91.4	90.9	190	4	47
3	7.1	16.2	96.3	95.7	200	4	45
4	7.5	17.0	101.1	100.5	210	4	42
5	7.8	17.8	105.8	105.2	220	4	40
6	11.4	26.0	154.0	153.1	320	25	28
7	14.9	34.1	202.1	200.9	420	19	21
8	18.5	42.2	250.1	248.7	520	15	17
9	22.0	50.3	298.3	296.6	620	15	14

Figure 6 shows examples of networks generated for backward and forward simulations with parameters used for numerical simulations. The small network, with sizes $5.4 \times 5.4 \times 10.8$ mm^3, contains 54,000 pores bodies and the large network, with sizes $9 \times 9 \times 50$ mm^3, contains over 250,000 pores.
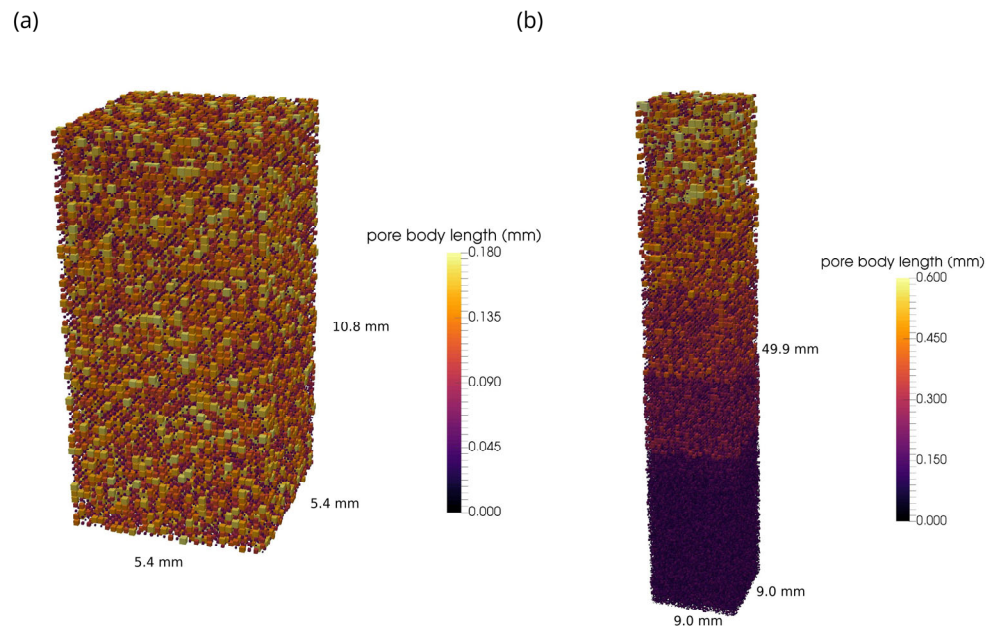
(a)   (b)

Figure 6. Examples of the network used in the case with networks generated for $\theta = \pi/4$. Only pore bodies are shown. (**a**) The small network with 54,000 pore bodies was used for backward simulation. (**b**) The large network with 253,146 pore bodies was utilized for forward simulation.

3.2. Results of the Simulation in a Small Network

A comparison of the simulated and measured retention curves is shown in Figure 7. A better agreement was obtained for $\theta = \pi/4$ with porosity close to the measured value.
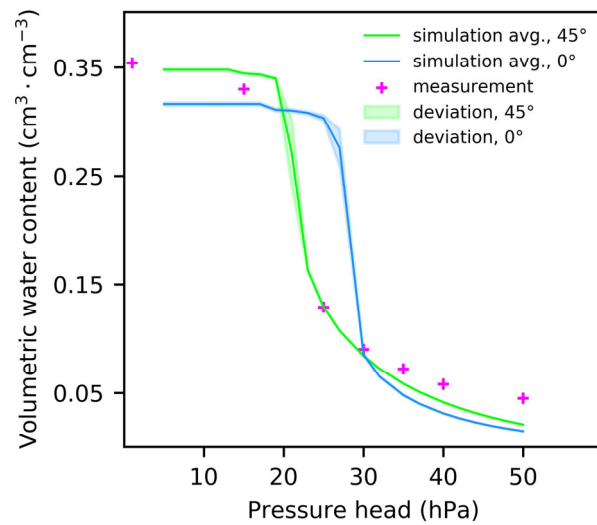
Figure 7. Comparison of the measured retention curve with the set of simulated retention curves. The simulated volumetric water contents were averaged for the corresponding pressure head values. The lines show the average of all 20 values, and the shaded area shows the standard deviation.

Furthermore, the relationships between the residual gas saturation of the satiated sample, $S_{g,r}$ (-), and the initial gas saturation, $S_{g,init}$ (-), are shown in Figure 8a. The maximum of $S_{g,r}$ was equal to 0.45 for $\theta = 0$ and 0.52 for $\theta = \pi/4$. The dotted lines show the fit of the quadratic model by [57]. There is an approximately linear growth of $S_{g,r}(S_{g,init})$ for lower values of initial gas saturation to the value over 0.5. Furthermore, the growth rate of the amount of entrapped air decreases significantly as the initial gas saturation increases. The general shape of the relationship is in good agreement with the findings of Pentland [58] and Kazemi [59]. Figure 8b shows the difference between the air distributions in the networks created for both contact angles for pressure head equal to 30 hPa.
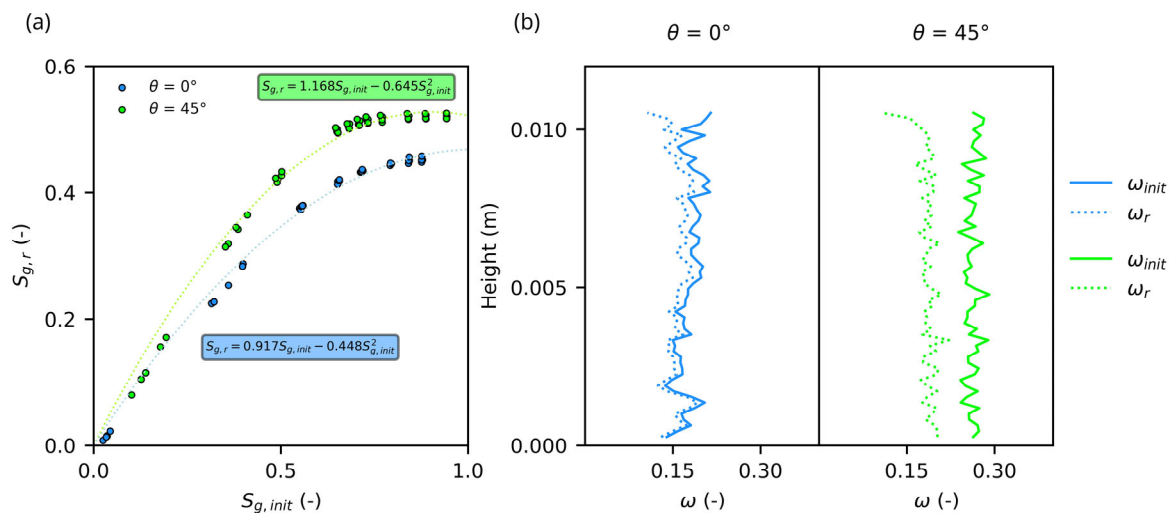

Figure 8. Comparison of the results for the backward simulation in a small network obtained using different networks generated for given contact angle θ. (**a**) Relationship $S_{g,r}(S_{g,init})$; $S_{g,init}$ is obtained from the drainage simulation, $S_{g,r}$ corresponds to the amount of air trapped. The results of five generated networks for each contact angle are shown. (**b**) Distribution of air in the sample. The solid line corresponds to the state after drainage with a pressure head of 30 hPa and the dotted line corresponds to the distribution of trapped air. In this case, a network was used.

3.3. Results of the Forward Simulation in a Large Network

The results are summarized in Table 2, where *SD* indicates the standard deviation. The mean and *SD* in rows were calculated from five different networks. The mean value of the volumetric air content ω within the entire sample determined by the simulation with the network generated for the contact angle $\pi/4$ is 0.34 after drainage and 0.18 after spontaneous imbibition. The mean value of ω in the case with a network generated for the contact angle 0 is 0.24 after drainage and 0.14 after spontaneous imbibition. The ω determined gravimetrically was 0.244 after drainage and 0.040 after the infiltration experiment. A linear approximation was used instead of a specific measurement. A linear approximation with the equation $S_{g,r} = 0.36 \cdot S_{g,init}$ can be used as it was determined in [55]. Then, the residual saturation, $S_{g,r}$, the estimate would be 0.23, which corresponds to the value of ω_r equal to 0.083. This way, we can say that the values of ω in the case with the network generated for $\theta = 0$ are relatively accurate.

Table 2. Summarized results for simulations in a large network. The results were obtained from five networks for each contact angle. *SD* indicates the standard deviation. The mean and *SD* values were calculated from these networks.

θ		$K(\omega_{g,r})$	$\omega_{g,init}$	$\omega_{g,r}$	AR	$SD(AR)$
		$\mathbf{cm \cdot s^{-1}}$	$\mathbf{cm^3 \cdot cm^{-3}}$	$\mathbf{cm^3 \cdot cm^{-3}}$	-	-
0	mean	0.035	0.24	0.12	1.88	1.59
	SD	1.5×10^{-4}	1.0×10^{-3}	1.5×10^{-3}	2.9×10^{-3}	6.0×10^{-3}
$\pi/4$	mean	0.035	0.34	0.18	1.55	0.82
	SD	3.8×10^{-4}	1.1×10^{-3}	1.3×10^{-3}	7.3×10^{-4}	1.1×10^{-3}

The air distribution in the sample, represented as volumetric air content (ω), is shown in Figure 9. Figure 9a presents the simulation results, while Figure 9b shows the adjusted results where, to account for small pores missed by µCT, gas-filled pores and throats smaller than 170 µm were excluded. This air content was used to compare with µCT results. Figure 9a indicates a relatively uniform air distribution across the height, unlike µCT images, where higher ω_r values appear in the upper half. This difference is due to larger, easily detectable air bubbles in the upper part, while smaller bubbles in the lower part were not well captured by µCT. The pore network model, however, reflects the total air content.

The effect that can influence the value of ω_r is the mobility of entrapped air bubbles that was not considered in the model. It is reasonable to assume that the ganglia could be mobile and capable of escaping the network even after capture. Figure 10 shows the distribution of the air clusters by size; approximately 50% of the number of individual air clusters are single-pore bubbles. However, the total volume of single-pore bubbles represents only approximately one hundredth of the sample volume.

The overestimated simulated value of ω_r cannot be attributed to the neglected snap-off mechanism because the use of the mechanism generally leads to higher ω_r values [17] and the snap-off mechanism is suppressed due to the low aspect ratio value [60], where the aspect ratio means the relationship between the pore body radius and pore throat radius. The average aspect ratio for the network generated for $\theta = \pi/4$ is 1.55 with a standard deviation 0.82 and for the network generated for $\theta = 0$ the average aspect ratio is 1.88 with a standard deviation of 1.59.

Our simulation results align well with the microtomography experimental work on sandstone published by Herring et al. [61], who also observed an increase in residual non-wetting phase content with rising contact angles (from strongly water-wet to weakly water-wet conditions). The increase in residual non-wetting phase is attributed to the dominance of capillary over viscous and gravitational forces within the contact angle range of 0 to $\pi/4$. This dominance shapes the drainage patterns, resulting in a higher content of non-wetting fluid as compared to the initial condition. During imbibition, a significant

amount of this non-wetting fluid becomes entrapped due to capillary forces acting on the non-uniform wetting front.
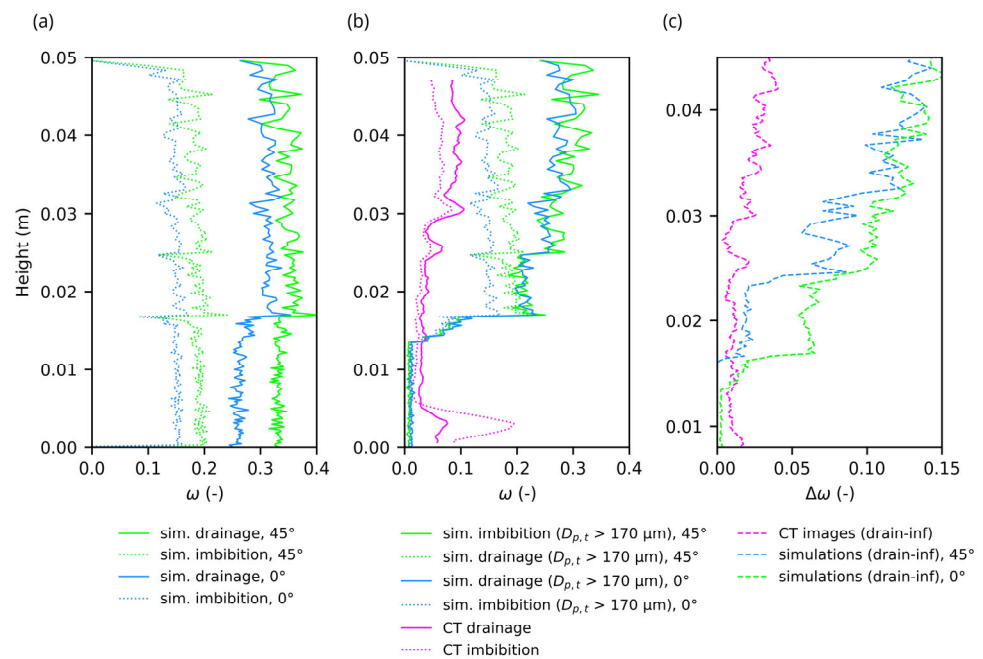

Figure 9. Air distribution in the sample. (**a**) The results obtained from the simulation. (**b**) The filtered results of the simulations correspond to only large μCT images determined air filled pores. The violet line shows the result obtained from μCT images. (**c**) Comparison of the difference between the volumetric air content obtained after drainage and after imbibition.
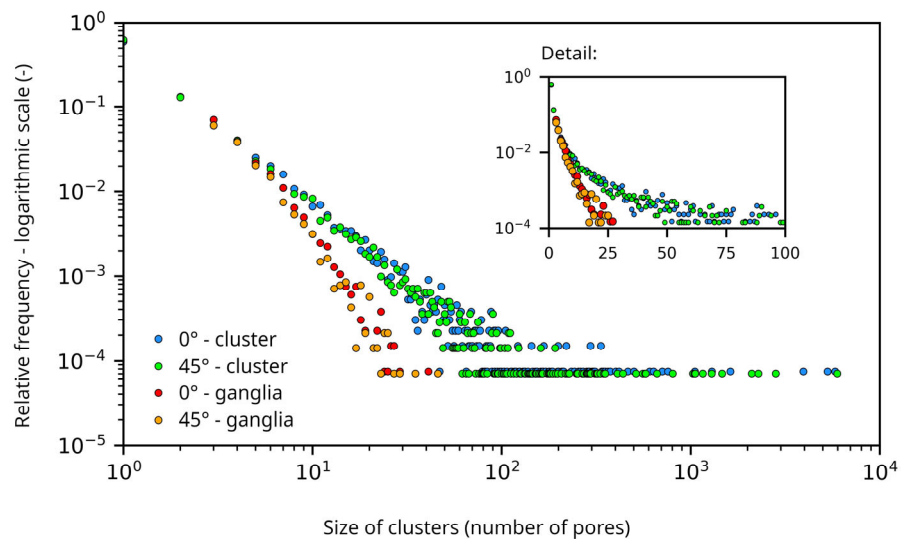

Figure 10. Relative frequency of the entrapped air clusters by size. Both axes have logarithmic scales. The embedded graph depicts details for the size of a cluster of less than 100 pore bodies. This detail has an x-axis with linear scale.

The value of K_s was obtained from the simulation in a small network where $K_s = 0.058$ cm·s^{-1} for the network generated for $\theta = \pi/4$ and $K_s = 0.045$ cm·s^{-1} for the network generated for $\theta = 0$. The low K_s value in the latter case is probably related to a lower porosity. The satiated hydraulic conductivity for a pressure head of 30 hPa was determined from simulation in a large network. The value is 0.035 cm·s^{-1} for the network generated for $\theta = \pi/4$ and 0.035 cm·s^{-1} for the network generated for $\theta = 0$. The measured value of

K_s was equal to 0.060 cm·s^{-1}. In our previous study [56], we experimentally determined $K(\omega_{max}) = 0.034$ cm·s^{-1} at a maximum obtained value of ω equal to 0.11. It can be seen in Figure 11 that the hydraulic conductivity for network generated for $\theta = 0$ was close to the measured value. However, saturated hydraulic conductivity was underestimated in the case when the $\theta = 0$ which is a consequence of lower porosity (see Figure 7).
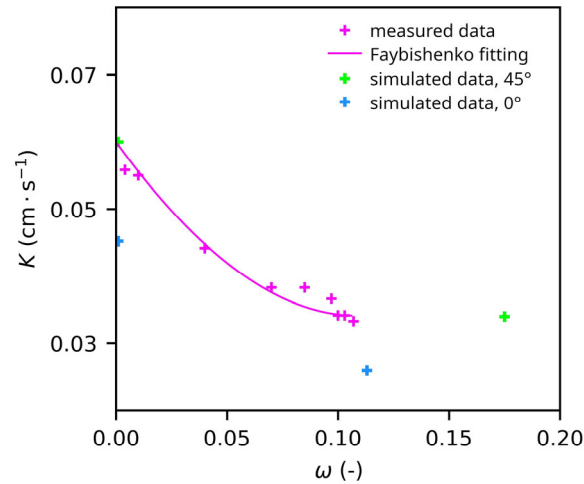

Figure 11. Relationship between volumetric air content and satiated hydraulic conductivity. Violet elements show measured data, and their fitting; lime and blue crosses show the results obtained by the simulations.

4. Conclusions

The simple pore-network model based on the OpenPNM platform was presented to simulate physical experiments with air trapping conducted on a sand sample. In the first numerical experiment, with a small uniform network, the network parameters were optimized to fit the measured retention curve and saturated hydraulic conductivity. The regular cubic network led to the best agreement with the measurement.

In the second case, the infiltration experiment performed on the sand column that was drained and subsequently filled with water from the bottom was simulated in a large non-uniform network composed of nine sub-networks. This simulation was performed without any further parameter optimization other than considering the pore network element size variability obtained from μCT images.

The model overestimated the amount of entrapped air for network generated for the contact angle $\pi/4$. The saturated hydraulic conductivity was determined with reasonable accuracy.

The case of network generated for contact angle of 0 provided relatively good agreement between the model and the measured content of air within the sample, but the saturated hydraulic conductivity was underestimated, which is probably a consequence of the presence of smaller pores and overall lower porosity obtained for this contact angle than the measured porosity. However, the satiated hydraulic conductivity reached a value similar to the measured value.

Limitations of this study are the assumptions of absence of entrapped gas buoyancy and snap-off mechanism. However, the latter only becomes relevant for simulations with larger contact angles than the ones considered here. Our study has demonstrated that fast quasi-static algorithms and a network that was generated using independently measured hydraulic properties together with additional information from μCT successfully capture trends of air entrapment during imbibition of sand in relation to the initial air saturation.

Author Contributions: T.P.: methodology (lead), formal analysis (lead), investigation (lead), data curation (lead), software (lead), writing—original draft (lead), writing—review and editing (equal), visualization (lead); J.K.: writing—review and editing (equal), investigation (equal); M.S.: conceptualization (lead), methodology (equal), writing—review and editing (equal), investigation (equal),

Appendix A Algorithms

Appendix A.1 Algorithm of Drainage

Drainage was modeled using the Invasion Percolation algorithm built into the OpenPNM platform. The result is then the list of the IDs of all the air-filled elements (pores and throats) for a given pressure head (ps_air and ts_air arrays). The IDs of the remaining pore bodies were stored in the ps_initial array, which represents pores filled with water in the initial state of the imbibition. The fraction of air in the pore bodies was determined as follows:

$$\omega = \frac{V_g}{V} = \left(\sum_{i \epsilon \textbf{ps\_air}} V_{p,i} + \sum_{j \epsilon \textbf{ts\_air}} V_{t,j} \right) / V$$

where ω (m^3·m^{-3}) is volumetric air content, V_g (m^3) is a volume of air present within the sample, V (m^3) is a volume of the whole sample, $V_{p,i}$ (m^3) is a volume of air in the pore body i, and $V_{t,j}$ (m^3) is a volume of air in the pore throat j. Volumes were determined by Equation (8). The ps_initial array was employed as an input in the algorithm of imbibition. Calculation of an imbibition algorithm in a large pore network took 1 to 2 min using desktop PC equipped with Intel i7 processor.

Appendix A.1.1 Algorithm of Imbibition

The difference between imbibition and drainage algorithms is that the entry pressure for the pore bodies is dependent on the occupancy of the surrounding throats. This affects the resulting geometry of the phase interface. As a result, the pore entry pressure may change at each step of the filling process. The IDs of pores bodies adjacent to the filled pore bodies were stored in the pores_neighbor array. In each step of the imbibition process, the pore body with maximum entry pressure from the pores_neighbor array was selected to be filled. The sequence number N_s was assigned to this pore, and N_s was increased by one. After this step, the pores adjacent to the newly filled pore were added to the pores_neighbor array. In these newly added pores, the entry pressure was updated according to the changing geometry of the air–water interface. The new entry pressure was determined by Equation (2).

Because of nonzero initial volumetric water content, some of the pore bodies were water-filled already at the beginning of the imbibition process (i.e., its ID was included in ps_initial). If the initially water-filled pore body appeared in the pores_neighbor array, then its filling (in the algorithm) has begun. The adjacent pores, which are also in the ps_initial array, were filled primarily regardless of the entry pressure.

The result of the imbibition algorithm is a pore-filling sequence, which then represents the input for the algorithm of entrapment.

Calculation of drainage algorithm in a large pore network took 10 to 15 h using desktop PC equipped with Intel i7 processor.

Appendix A.1.2 Algorithm of Entrapment

The algorithm used to calculate capillary air entrapment [23] was based on a similar one implemented in OpenPNM. We modified it to model the invading wetting phase. The input for the algorithm was the pore filling sequence and the array of initially water-filled ps_initial.

We used the bypass entrapment mechanism to delineate air entrapment by identifying air-filled pores that become surrounded by water-filled pores before they fill themselves [61]. In the process, clusters of pores with trapped air were formed during the imbibition simulation. Each cluster of trapped air is labeled from number 1 onwards. The cluster of air-filled pore bodies connected to the outlet was labeled 0. This cluster corresponds to pores that are in the end filled with water. At the beginning of the algorithm, all pores were labeled −1 to help identify pores that have not been processed by the algorithm.

The algorithm used the reverse sequence of the water pore filling, obtained from the imbibition algorithm. Generally, groups of connected pores filled with the defending phase (air) were created, and each group was labeled with a label number. Three situations could have occurred in each step when one goes backward in time [55]: (i) The number of clusters with defending phase stays the same—the cluster (with label 0 or greater) can grow, (ii) new cluster of size equal to one is created and assigned a new cluster label number, which is incremented by one, (iii) multiple clusters merge into one cluster with a single label number that is equal to the maximum of the label numbers of the merged clusters.

Only clusters of the defending phase that do not join the cluster connected to the outlet can grow and merge. Cluster growth stops when a neighboring pore connected to cluster 0 is reached. The pores of this cluster are imported into the ps_entrapped array. After the algorithm is completed for the entire network, the pores from ps_initial are removed from the ps_entrapped array, which now has its final form. It is assumed that only the pore throats between two pore bodies with trapped air can remain air filled at the end of the imbibition simulation. In this way, the ts_entrapped array is constructed. The amount of entrapped (residual) air, ω_r, was determined by the equation:

$$\omega_r = \frac{V_{g,entrapped}}{V} = \left(\sum_{i \epsilon \text{ps\_entrapped}} V_{p,i} + \sum_{j \epsilon \text{ts\_entrapped}} V_{t,j} \right) / V$$

The algorithm result was a list of pores that contain trapped air and the value of ω_r. Calculation of entrapment algorithm in a large pore network took up to 1 min using desktop PC equipped with Intel i7 processor.

Appendix A.1.3 Algorithm Determining the Flow

The satiated hydraulic conductivity was determined from the flow rate at a known hydraulic gradient. The boundary conditions were defined as constant pressure on the top and bottom boundaries and no flow over the other boundaries. The flowrate q_{ij} between pores is determined by Equation (9). The necessary phase pressures were determined by applying a volume conservation equation at each pore body:

$$\sum_j q_{ij} = 0$$

where the sum was performed on all adjacent pore bodies of pore body i. The pressure field was determined by solving the system of N_p equations, where N_p is the number of pore bodies in the whole network. The Stokes Flow algorithm from OpenPNM was used to calculate the flow. The hydraulic conductivity was then determined by Darcy's law:

$$K = \frac{Q}{A} \frac{L}{\Delta H}$$

where Q (m^3·s^{-1}) is the flow rate across the top and bottom boundaries, A (m^2) is the cross-sectional area, L (m) the length of the sample, and H (m) is the hydraulic head difference. In the case of the presence of entrapped air in the pore medium, the result corresponded to a satiated hydraulic conductivity, $K(\omega)$ (m·s^{-1}) with volumetric entrapped air content ω.

References

1. Faybishenko, B. Hydraulic Behavior of Quasi-Saturated Soils in The Presence of Entrapped Air—Laboratory Experiments. *Water Resour. Res.* **1995**, *31*, 2421–2435. [CrossRef]
2. Marinas, M.; Roy, J.W.; Smith, J.E. Changes in Entrapped Gas Content and Hydraulic Conductivity with Pressure. *Ground Water* **2013**, *51*, 41–50. [CrossRef] [PubMed]
3. Dohnal, M.; Jelinkova, V.; Snehota, M.; Dusek, J.; Brezina, J. Tree-Dimensional Numerical Analysis of Water Flow Affected by Entrapped Air: Application of Noninvasive Imaging Techniques. *Vadose Zone J.* **2013**, *12*, 1–12. [CrossRef]
4. Sacha, J.; Jelinkova, V.; Snehota, M.; Vontobel, P.; Hovind, J.; Cislerova, M. Water and Air Redistribution within a Dual Permeability Porous System Investigated Using Neutron Imaging. In Proceedings of the 10th World Conference on Neutron Radiography (WCNR-10), Grindelwald, Switzerland, 5–10 October 2014; Volume 69, pp. 530–536.
5. Snehota, M.; Jelinkova, V.; Sobotkova, M.; Sacha, J.; Vontobel, P.; Hovind, J. Water and Entrapped Air Redistribution in Heterogeneous Sand Sample: Quantitative Neutron Imaging of the Process. *Water Resour. Res.* **2015**, *51*, 1359–1371. [CrossRef]
6. Faust, C.R.; Guswa, J.H.; Mercer, J.W. Simulation of 3-Dimensional Flow of Immiscible Fluids within and below the Unsaturated Zone. *Water Resour. Res.* **1989**, *25*, 2449–2464. [CrossRef]
7. Scanziani, A.; Singh, K.; Menke, H.P.; Bijeljic, B.; Blunt, M.J. Dynamics of Enhanced Gas Trapping Applied to CO_2 Storage in the Presence of Oil Using Synchrotron X-Ray Micro Tomography. *Appl. Energy* **2020**, *259*, 114136. [CrossRef]
8. Wang, Z.; Pereira, J.-M.; Sauret, E.; Gan, Y. Wettability Impacts Residual Trapping of Immiscible Fluids During Cyclic Injection. *J. Fluid Mech.* **2023**, *961*, A19. [CrossRef]
9. Fucik, R.; Klinkovsky, J.; Solovsky, J.; Oberhuber, T.; Mikyska, J. Multidimensional Mixed-Hybrid Finite Element Method for, Compositional Two-Phase Flow in Heterogeneous Porous Media and Its Parallel Implementation on GPU. *Comput. Phys. Commun.* **2019**, *238*, 165–180. [CrossRef]
10. Wanfang, Z.; Wheater, H.S.; Johnston, P.M. State of the Art of Modelling Two-Phase Flow in Fractured Rock. *Environ. Geol.* **1997**, *31*, 157–166. [CrossRef]
11. Hilfer, R. Capillary Pressure, Hysteresis and Residual Saturation in Porous Media. *Phys. A-Stat. Mech. Its Appl.* **2006**, *359*, 119–128. [CrossRef]
12. Lenhard, R.J.; Parker, J.C.; Kaluarachchi, J.J. Comparing Simulated and Experimental Hysteretic 2-Phase Transient Fluid-Flow Phenomena. *Water Resour. Res.* **1991**, *27*, 2113–2124. [CrossRef]
13. Liu, Z.Y.; Wu, H.Y. Pore-Scale Modeling of Immiscible Two-Phase Flow in Complex Porous Media. *Appl. Therm. Eng.* **2016**, *93*, 1394–1402. [CrossRef]
14. Raeini, A.Q.; Bijeljic, B.; Blunt, M.J. Modelling Capillary Trapping Using Finite-Volume Simulation of Two-Phase Flow Directly on Micro-CT Images. *Adv. Water Resour.* **2015**, *83*, 102–110. [CrossRef]
15. Sukop, M.C.; Huang, H.; Lin, C.L.; Deo, M.D.; Oh, K.; Miller, J.D. Distribution of Multiphase Fluids in Porous Media: Comparison between Lattice Boltzmann Modeling and Micro-x-Ray Tomography. *Phys. Rev. E* **2008**, *77*, 026710. [CrossRef] [PubMed]
16. Joekar-Niasar, V.; Hassanizadeh, S.M. Analysis of Fundamentals of Two-Phase Flow in Porous Media Using Dynamic Pore-Network Models: A Review. *Crit. Rev. Environ. Sci. Technol.* **2012**, *42*, 1895–1976. [CrossRef]
17. Mahmud, W.M.; Nguyen, V.H. Effects of Snap-off in Imbibition in Porous Media with Different Spatial Correlations. *Transp. Porous Media* **2006**, *64*, 279–300. [CrossRef]
18. Porter, M.L.; Schaap, M.G.; Wildenschild, D. Lattice-Boltzmann Simulations of the Capillary Pressure-Saturation-Interfacial Area Relationship for Porous Media. *Adv. Water Resour.* **2009**, *32*, 1632–1640. [CrossRef]
19. Blunt, M.J.; Bijeljic, B.; Dong, H.; Gharbi, O.; Iglauer, S.; Mostaghimi, P.; Paluszny, A.; Pentland, C. Pore-Scale Imaging and Modelling. *Adv. Water Resour.* **2013**, *51*, 197–216. [CrossRef]
20. Kohne, J.M.; Schluter, S.; Vogel, H.J. Predicting Solute Transport in Structured Soil Using Pore Network Models. *Vadose Zone J.* **2011**, *10*, 1082–1096. [CrossRef]
21. Oostrom, M.; Mehmani, Y.; Romero-Gomez, P.; Tang, Y.; Liu, H.; Yoon, H.; Zhang, C. Pore-Scale and Continuum Simulations of Solute Transport Micromodel Benchmark Experiments. *Comput. Geosci.* **2016**, *20*, 857–879. [CrossRef]
22. Hunt, A.G. Basic Transport Properties in Natural Porous Media—Continuum Percolation Theory and Fractal Model. *Complexity* **2005**, *10*, 22–37. [CrossRef]
23. Masson, Y.; Pride, S.R. A Fast Algorithm for Invasion Percolation. *Transp. Porous Media* **2014**, *102*, 301–312. [CrossRef]
24. Geistlinger, H.; Mohammadian, S. Capillary Trapping Mechanism in Strongly Water Wet Systems: Comparison between Experiment and Percolation Theory. *Adv. Water Resour.* **2015**, *79*, 35–50. [CrossRef]
25. Ghanbarian, B.; Daigle, H.; Hunt, A.G.; Ewing, R.P.; Sahimi, M. Gas and Solute Diffusion in Partially Saturated Porous Media: Percolation Theory and Effective Medium Approximation Compared with Lattice Boltzmann Simulations. *J. Geophys. Res.-Solid Earth* **2015**, *120*, 182–190. [CrossRef]

26. Ghanbarian, B.; Hunt, A.G.; Sahimi, M.; Ewing, R.P.; Skinner, T.E. Percolation Theory Generates a Physically Based Description of Tortuosity in Saturated and Unsaturated Porous Media. *Soil Sci. Soc. Am. J.* **2013**, *77*, 1920–1929. [CrossRef]

27. Kohanpur, A.H.; Chen, Y.; Valocchi, A.J. Using Direct Numerical Simulation of Pore-Level Events to Improve Pore-Network Models for Prediction of Residual Trapping of CO_2. *Front. Water* **2022**, *3*, 710160. [CrossRef]

28. Rebai, M.; Prat, M. Scale Effect and Two-Phase Flow in a Thin Hydrophobic Porous Layer. Application to Water Transport in Gas Diffusion Layers of Proton Exchange Membrane Fuel Cells. *J. Power Sources* **2009**, *192*, 534–543. [CrossRef]

29. Liu, X.L.; Peng, C.; Bai, H.X.; Zhang, Q.F.; Ye, G.H.; Zhou, X.G.; Yuan, W.K. A Pore Network Model for Calculating Pressure Drop in Packed Beds of Arbitrary-Shaped Particles. *AIChE J.* **2020**, *66*, e16258. [CrossRef]

30. Sahimi, M. Flow Phenomena in Rocks: From Continuum Models to Fractals, Percolation, Cellular Automata, and Simulated Annealing. *Rev. Mod. Phys.* **1993**, *65*, 1393–1534. [CrossRef]

31. Vogel, H.J.; Roth, K. Quantitative Morphology and Network Representation of Soil Pore Structure. *Adv. Water Resour.* **2001**, *24*, 233–242. [CrossRef]

32. Blunt, M.; King, M.J.; Scher, H. Simulation and Theory of Two-Phase Flow in Porous Media. *Phys. Rev. A* **1992**, *46*, 7680–7699. [CrossRef] [PubMed]

33. Fatt, I. The Network Model of Porous Media.1. Capillary Pressure Characteristics. *Trans. Am. Inst. Min. Metall. Eng.* **1956**, *207*, 144–159.

34. Lenormand, R.; Zarcone, C.; Sarr, A. Mechanisms of the Displacement of One Fluid by Another in a Network of Capillary Ducts. *J. Fluid Mech.* **1983**, *135*, 337–353. [CrossRef]

35. Fischer, U.; Celia, M.A. Prediction of Relative and Absolute Permeabilities for Gas and Water from Soil Water Retention Curves Using a Pore-Scale Network Model. *Water Resour. Res.* **1999**, *35*, 1089–1100. [CrossRef]

36. Meyer, D.W. Random Generation of Irregular Natural Flow or Pore Networks. *Adv. Water Resour.* **2021**, *152*, 103936. [CrossRef]

37. Raoof, A.; Hassanizadeh, S.M. A New Method for Generating Pore-Network Models of Porous Media. *Transp. Porous Media* **2010**, *81*, 391–407. [CrossRef]

38. Dong, H.; Blunt, M.J. Pore-Network Extraction from Micro-Computerized-Tomography Images. *Phys. Rev. E* **2009**, *80*, 036307. [CrossRef] [PubMed]

39. Silin, D.; Tomutsa, L.; Benson, S.M.; Patzek, T.W. Microtomography and Pore-Scale Modeling of Two-Phase Fluid Distribution. *Transp. Porous Media* **2011**, *86*, 525–545. [CrossRef]

40. Xiong, Q.R.; Baychev, T.G.; Jivkov, A.P. Review of Pore Network Modelling of Porous Media: Experimental Characterisations, Network Constructions and Applications to Reactive Transport. *J. Contam. Hydrol.* **2016**, *192*, 101–117. [CrossRef]

41. Al-Raoush, R.I.; Willson, C.S. Extraction of Physically Realistic Pore Network Properties from Three-Dimensional Synchrotron X-Ray Microtomography Images of Unconsolidated Porous Media Systems. *J. Hydrol.* **2005**, *300*, 44–64. [CrossRef]

42. Piovesan, A.; Van De Looverbosch, T.; Verboven, P.; Achille, C.; Cabrera, C.P.; Boller, E.; Nicolai, B. 4D Synchrotron Microtomography and Pore-Network Modelling for Direct in Situ Capillary Flow Visualization in 3D Printed Microfluidic Channels. *Lab Chip* **2020**, *20*, 2403–2411. [CrossRef] [PubMed]

43. Hefny, M.; Qin, C.Z.; Saar, M.O.; Ebigbo, A. Synchrotron-Based Pore-Network Modeling of Two-Phase Flow in Nubian Sandstone and Implications for Capillary Trapping of Carbon Dioxide. *Int. J. Greenh. Gas Control* **2020**, *103*, 103164. [CrossRef]

44. Gostick, J.; Aghighi, M.; Hinebaugh, J.; Tranter, T.; Hoeh, M.A.; Day, H.; Spellacy, B.; Sharqawy, M.H.; Bazylak, A.; Burns, A.; et al. OpenPNM: A Pore Network Modeling Package. *Comput. Sci. Eng.* **2016**, *18*, 60–74. [CrossRef]

45. Chevalier, S.; Hinebaugh, J.; Bazylak, A. Establishing Accuracy of Watershed-Derived Pore Network Extraction for Characterizing In-Plane Effective Diffusivity in Thin Porous Layers. *J. Electrochem. Soc.* **2019**, *166*, F3246–F3254. [CrossRef]

46. Aghighi, M.; Hoeh, M.A.; Lehnert, W.; Merle, G.; Gostick, J. Simulation of a Full Fuel Cell Membrane Electrode Assembly Using Pore Network Modeling. *J. Electrochem. Soc.* **2016**, *163*, F384–F392. [CrossRef]

47. Tranter, T.G.; Gostick, J.T.; Burns, A.D.; Gale, W.F. Pore Network Modeling of Compressed Fuel Cell Components with OpenPNM. *Fuel Cells* **2016**, *16*, 504–515. [CrossRef]

48. Ma, S.X.; Mason, G.; Morrow, N.R. Effect of Contact Angle on Drainage and Imbibition in Regular Polygonal Tubes. *Colloids Surf. A-Physicochem. Eng. Asp.* **1996**, *117*, 273–291. [CrossRef]

49. Ruspini, L.C.; Farokhpoor, R.; Oren, P.E. Pore-Scale Modeling of Capillary Trapping in Water-Wet Porous Media: A New Cooperative Pore-Body Filling Model. *Adv. Water Resour.* **2017**, *108*, 1–14. [CrossRef]

50. Joekar-Niasar, V.; Hassanizadeh, S.M.; Leijnse, A. Insights into the Relationships among Capillary Pressure, Saturation, Interfacial Area and Relative Permeability Using Pore-Network Modeling. *Transp. Porous Media* **2008**, *74*, 201–219. [CrossRef]

51. Bryant, S.; Blunt, M. Prediction of Relative Permeability in Simple Porous-Media. *Phys. Rev. A* **1992**, *46*, 2004–2011. [CrossRef]

52. Hughes, R.G.; Blunt, M.J. Pore Scale Modeling of Rate Effects in Imbibition. *Transp. Porous Media* **2000**, *40*, 295–322. [CrossRef]

53. Zhou, D.G.; Blunt, M.; Orr, F.M. Hydrocarbon Drainage along Corners of Noncircular Capillaries. *J. Colloid Interface Sci.* **1997**, *187*, 11–21. [CrossRef] [PubMed]

54. Klute, A. Water Retention: Laboratory Methods. In *Methods of Soil Analysis—Part 1—Physical and Mineralogical Methods*; Soil Science Society of America: Madison, WI, USA, 1986; pp. 635–662.

55. Princ, T.; Fideles, H.M.R.; Koestel, J.; Snehota, M. The Impact of Capillary Trapping of Air on Satiated Hydraulic Conductivity of Sands Interpreted by X-Ray Microtomography. *Water* **2020**, *12*, 445. [CrossRef]

56. Van Genuchten, M.T. A Closed-Form Equation for Predicting the Hydraulic Conductivity of Unsaturated Soils. *Soil Sci. Soc. Am. J.* **1980**, *44*, 892–898. [CrossRef]

57. Spiteri, E.J.; Juanes, R.; Blunt, M.J.; Orr, F.M. A New Model of Trapping and Relative Permeability Hysteresis for All Wettability Characteristics. *SPE J.* **2008**, *13*, 277–288. [CrossRef]

58. Pentland, C.H.; Itsekiri, E.; Al Mansoori, S.K.; Iglauer, S.; Bijeljic, B.; Blunt, M.J. Measurement of Nonwetting-Phase Trapping in Sandpacks. *SPE J.* **2010**, *15*, 274–281. [CrossRef]

59. Kazemi, F.; Azin, R.; Osfouri, S. Evaluation of Phase Trapping Models in Gas-Condensate Systems in an Unconsolidated Sand Pack. *J. Pet. Sci. Eng.* **2020**, *195*, 107848. [CrossRef]

60. Chatzis, I.; Morrow, N.R.; Lim, H.T. Magnitude and Detailed Structure of Residual Oil Saturation. *Soc. Pet. Eng. J.* **1983**, *23*, 311–326. [CrossRef]

61. Herring, A.L.; Sheppard, A.; Andersson, L.; Wildenschild, D. Impact of Wettability Alteration on 3D Nonwetting Phase Trapping and Transport. *Int. J. Greenh. Gas Control* **2016**, *46*, 175–186. [CrossRef]